



HAL
open science

Landsat Snow-Free Surface Albedo Estimation Over Sloping Terrain: Algorithm Development and Evaluation

Yichuan Ma, Tao He, Shunlin Liang, Jianguang Wen, Jean-Philippe Gastellu-Etchegorry, Jiang Chen, Anxin Ding, Siqi Feng

► To cite this version:

Yichuan Ma, Tao He, Shunlin Liang, Jianguang Wen, Jean-Philippe Gastellu-Etchegorry, et al.. Landsat Snow-Free Surface Albedo Estimation Over Sloping Terrain: Algorithm Development and Evaluation. IEEE Transactions on Geoscience and Remote Sensing, 2022, 60, pp.1-14. 10.1109/TGRS.2022.3149762 . hal-04644086

HAL Id: hal-04644086

<https://hal.science/hal-04644086>

Submitted on 12 Jul 2024

HAL is a multi-disciplinary open access archive for the deposit and dissemination of scientific research documents, whether they are published or not. The documents may come from teaching and research institutions in France or abroad, or from public or private research centers.

L'archive ouverte pluridisciplinaire **HAL**, est destinée au dépôt et à la diffusion de documents scientifiques de niveau recherche, publiés ou non, émanant des établissements d'enseignement et de recherche français ou étrangers, des laboratoires publics ou privés.



Distributed under a Creative Commons Attribution - NonCommercial - NoDerivatives 4.0 International License

Landsat Snow-Free Surface Albedo Estimation Over Sloping Terrain: Algorithm Development and Evaluation

Yichuan Ma¹, Tao He¹, *Member, IEEE*, Shunlin Liang², *Fellow, IEEE*, Jianguang Wen, Jean-Philippe Gastellu-Etchegorry, *Member, IEEE*, Jiang Chen³, Anxin Ding³, and Siqi Feng

Abstract—Surface albedo plays a key role in global climate modeling as a factor controlling the energy budget. Satellite observations were utilized to estimate surface albedo at global and regional scales with good precision over flat areas. However, because topography greatly complicates radiative transfer (RT) processes, estimating the albedo of rugged terrain with satellite data remains a challenge. In addition, albedo definitions over sloping terrain differ from that for flat areas. They include horizontal/horizontal sloped surface albedo (HHSA) and inclined/inclined sloped surface albedo (IISA). Methods for retrieving HHSA and IISA in mountains have not been well-explored. Here, we retrieved HHSA and IISA on sloping terrain from Landsat 8 using a direct estimation algorithm. We simulated a dataset of Landsat top-of-atmosphere (TOA) reflectance and surface albedo with discrete anisotropic radiative transfer (DART) model, for variable atmospheric, vegetation, soil, and topography properties. Then, we used artificial neural networks (ANNs) to derive an empirical relationship between TOA reflectance and surface albedo. The accuracy of our method was verified with *in situ* measurements: root mean squared error (RMSE) and bias equal to 0.029 and -0.010 for HHSA, and 0.023 and -0.001 for IISA, respectively. Several albedo results (HHSA, IISA, values without topographic consideration) were evaluated and compared. HHSA was found similar to albedo without topographic consideration, but IISA, considered as the “true albedo” for sloping terrain, showed large difference from them. This study demonstrated the feasibility of surface albedo estimation from Landsat TOA reflectance directly in rugged terrains and advanced our understanding of energy budget in mountains.

Index Terms—Artificial neural network (ANN), direct estimation algorithm, Landsat, discrete anisotropic radiative transfer (DART), sloping terrain, surface albedo.

I. INTRODUCTION

MOUNTAINS cover approximately a quarter of earth’s land surface [1], with 25% of terrestrial biodiversity and 28% of global forests [2]. Their ecosystems are fragile and sensitive to climate change; the mechanisms of which, however, have not been well explored [3]–[5]. Among which, monitoring mountain energy budget is of great importance for understanding global and regional climate change [6], [7].

Surface albedo, defined as the ratio of reflected to incident shortwave radiation, is a primary controlling factor for global energy budget and is usually a key variable in climate models [8]. Satellite remote sensing is widely used as the most effective way to estimate surface albedo in large areas with long time series. Many albedo estimation algorithms [9]–[11] and global products [12]–[15] have been developed, which has boosted climate change research [16]–[18]. In recent years, fine spatial resolution (e.g., 10–50 m, hereinafter be shorted as “fine-resolution”) albedo estimation algorithms and datasets have been developed for fine-scale environmental monitoring and ecological applications [10], [19], [20], with a good potential for better understanding and quantifying energy budget in mountainous areas.

Topographic effects change the sun-target-viewing geometrics, and it greatly influenced incoming and reflected radiative fluxes in mountains [21], [22] (up to 600 W/m²), and thus impacted surface albedo obviously; and negligence of such effects for surface albedo retrievals over mountain areas could introduce large errors [23], [24]. For example, Wen *et al.* [25] showed that the coarse-scale albedo error can reach 33% over a 40° slope. Hao *et al.* [23] highlighted the need to consider topographic effects on snow-free surface albedo even over a gentle terrain (with slope of 10°–20°). Shi and Xiao [26] found that the errors could exceed 35% when ignoring topographic effects for surface albedo in rugged terrain. Therefore, the consideration of topography is necessary when estimating surface albedo in mountainous areas. Meanwhile, there are two definitions of surface albedo of sloping terrain [27], [28]: horizontal/horizontal sloped surface albedo (HHSA) and inclined/inclined sloped surface albedo

Manuscript received November 22, 2021; revised January 13, 2022; accepted January 31, 2022. Date of publication February 7, 2022; date of current version March 23, 2022. This work was supported in part by the National Key Research and Development Program of China under Grant 2020YFA0608704 and in part by the National Natural Science Foundation of China under Grant 42090012 and Grant 41771379. (*Corresponding author: Tao He.*)

Yichuan Ma, Tao He, Jiang Chen, Anxin Ding, and Siqi Feng are with the School of Remote Sensing and Information Engineering, Wuhan University, Wuhan 430079, China (e-mail: ma_yichuan@whu.edu.cn; taohers@whu.edu.cn; chenjiang@whu.edu.cn; danxin@whu.edu.cn; siqi_feng@whu.edu.cn).

Shunlin Liang is with the Department of Geographical Sciences, University of Maryland at College Park, College Park, MD 20742 USA (e-mail: sliang@umd.edu).

Jianguang Wen is with the State Key Laboratory of Remote Sensing Science, Aerospace Information Research Institute, Chinese Academy of Sciences, Beijing 100101, China (e-mail: wenjg@aircas.ac.cn).

Jean-Philippe Gastellu-Etchegorry is with the Center d’Etudes Spatiales de la Biosphere, Paul Sabatier University, 31062 Toulouse, France (e-mail: jean-philippe.gastellu-etchegorry@cesbio.cnrs.fr).

Digital Object Identifier 10.1109/TGRS.2022.3149762

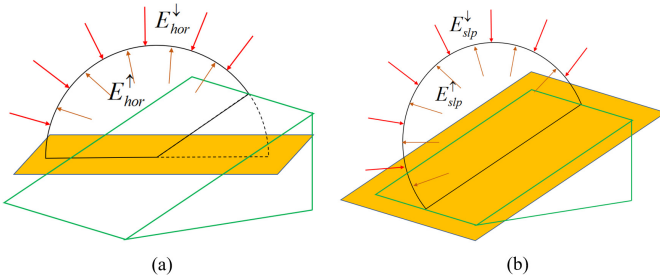


Fig. 1. (a) HHSA and (b) IISA on sloping terrain. The yellow rectangles indicate the reference planes. The black sectors indicate the angular range of incident radiation for different albedos.

TABLE I
MAIN DIFFERENCE AMONG DIFFERENT ALBEDO DEFINITIONS

Albedo names	Definition difference	Application difference
Albedo on flat areas	The ratio of upward radiation to downward radiation, and not includes reflected radiation from nearby environment.	In flat areas.
HHSA	Use the horizontal plane as the reference plane, and reflected radiation from nearby environment is included in both upward and downward radiation.	More correlated with the vegetation properties when it comes to single trees and tree clusters [32].
IISA	Use the sloping terrain as the reference plane, and the downward and upward radiation in this definition are consistent with the radiation reach and reflected from the ground.	Considered as the physically correct meaning of the albedo on sloping terrain [27, 33].

(IISA, also called slope-parallel albedo), as shown in Fig. 1. The mathematical definitions for HHSA and IISA are shown in the following equations:

$$\text{HHSA} = E_{\text{hor}}^{\uparrow} / E_{\text{hor}}^{\downarrow} \quad (1)$$

$$\text{IISA} = E_{\text{slp}}^{\uparrow} / E_{\text{slp}}^{\downarrow} \quad (2)$$

where $E_{\text{hor}}^{\uparrow}$ and $E_{\text{hor}}^{\downarrow}$ are upward and downward shortwave radiation on horizontal plane and $E_{\text{slp}}^{\uparrow}$ and $E_{\text{slp}}^{\downarrow}$ are on the sloping terrain, and mathematical details were described in [28]. The main difference between HHSA and IISA is concluded in Table I. The confusion of HHSA and IISA may lead to large deviations in further studies markedly, such as net radiation retrieval [29] and small-scale fire process analysis in mountains [30], [31]. Therefore, it is in urgent need to advance our knowledge about HHSA and IISA in large areas to better understand mountainous ecosystem.

Some studies have been carried out to estimate surface albedo over mountainous areas. To correct the topographic effects in coarse-scale albedo data, Wen *et al.* [25], [34] smoothed the topography in the coarse-scale pixel and developed an equivalent slope for moderate-resolution imaging spectroradiometer (MODIS) albedo estimation. To obtain daily albedo in mountains, Li *et al.* [35] retrieved the shadow cov-

erage ratio for the correction of beam radiance, and estimated albedo on complex terrain using MODIS data. To overcome the topographic effects in high-resolution data, Shi *et al.* [36] employed a coupled surface-atmosphere model with topographic consideration, and estimated multiple parameters in rugged terrain, including HHSA. To cover the gap of albedo product in high latitude, Traversa *et al.* [37] obtained albedo based on atmospheric and topographic correction, and narrow-to-broadband conversion. Lin *et al.* [38] found that retrieving albedo by bidirectional reflectance distribution function (BRDF)-based mountain-radiative-transfer (RT) model was more accurate than retrieving it using separate atmospheric and topographic corrections in mountains. Ma *et al.* [39] also found correction bias in the widely used topographic correction models, and recommended coupling topographic considerations in parameters estimation rather than adopt topographic correction. Some researchers have developed conversion algorithms from HHSA to IISA for *in situ* measurements [33], [40], but studies for both HHSA and IISA estimation from satellite data are still lacking.

Fine-resolution satellites have the potential to depict surface albedo in mountainous areas because topography induces large spatial variability. However, their relatively small field of views, long revisit cycles, and rapid change of sun-target-sensor geometry in mountains make it difficult to collect enough BRDF samplings to follow the albedo estimation procedure with coarse-resolution satellite data, such as the MODIS albedo product algorithm [12], [15], [41]. In addition, performing atmospheric corrections in mountainous areas is difficult, and the adoption of topographic correction and atmospheric correction would introduce errors into albedo estimation. The direct estimation algorithm [9] could be used to estimate surface albedo from top-of-atmosphere (TOA) reflectance with instantaneous observations, and has shown good performance in global scale [42], [43]. It also showed great potential for accurate surface albedo estimation from satellite data with limited angular sampling, such as Airborne Visible Infrared Imaging Spectrometer [44], Chinese HJ-1 [45], and Landsat [46]. In mountainous areas, the direct estimation algorithm may be a good option to retrieve albedo without explicit atmospheric correction and BRDF modeling. The recent improved accuracy and computing efficiency of 3-D RT models [47], [48] and high-performance computers offer us new opportunities for direct estimation of HHSA and IISA on sloping terrain. Furthermore, there are remaining problems in albedo estimation in mountains.

1) How to design the simulation scene and select appropriate parameters to simulate typical sloping terrain?

2) How to utilize the simulation dataset for high-resolution albedo estimation in mountains?

3) Whether it is possible to estimate HHSA and IISA from satellite observations?

4) What is the difference between albedo with different definitions?

The main objectives of this article are to explore the feasibility of direct estimation algorithm based on the state-of-the-art 3-D RT model that estimates snow-free albedo of sloping terrain with fine-resolution TOA satellite reflectance

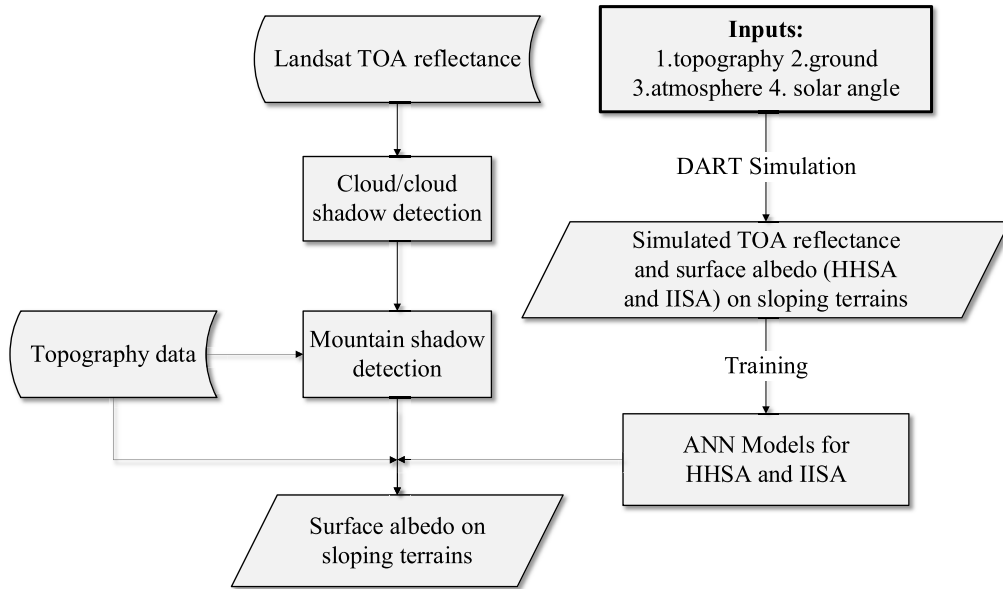


Fig. 2. Flowchart of surface albedo estimation on sloping terrain with the direct estimation algorithm.

and topography data, and also to evaluate and compare different surface albedo over mountain areas. The following strategies assured our model's robustness.

1) Global sensitivity analysis was used to select typical simulation parameters which ensured the simulation datasets representativeness.

2) Good validation results against simulation dataset and ground measurements declared our model's feasibility in diverse conditions.

The methods and data are included in Sections II and III, respectively. The albedo estimation results are presented in Section IV and discussed in Section V. Finally, the conclusions are provided in Section VI.

II. METHODOLOGY

The discrete anisotropy radiative transfer (DART) [48] model was used for atmospheric and sloping terrain's RT modeling. Artificial neural network (ANN) models were used to link solar angles, topography, simulated TOA reflectance, and surface albedo. ANN models were applied to satellite observations and topographic data for HHSA and IISA estimations, respectively. We validated results with both simulated dataset and *in situ* measurements, and we compared and analyzed the albedo estimation without considering the topographic effects [46], and the estimated HHSA and IISA.

Fig. 2 shows the flowchart of our surface albedo estimation on sloping terrain. First, DART simulations were carried out for creating a simulation dataset, with consideration of topography, surface reflectivity properties (soil and vegetation), atmospheric conditions, and illumination-viewing geometries; their typical parameters setting in this study was adopted from former studies [23], [49], [50] followed by sensitivity analyses. Second, sun zenith angle (SZA), slope, relative angle between sun azimuth angle and terrain's aspect (RAA), and TOA reflectance and surface albedo (HHSA and

IISA, respectively) were used for constructing ANN models. We used 75% simulations to build ANN models, and 25% to validate the models. We also collected *in situ* measured HHSA and IISA for validation. Then, in the preprocessing step of Landsat TOA reflectance data, pixels with cloud and shadow were removed. Finally, surface albedo was estimated by supplying the topographic data and satellite (e.g., Landsat) TOA reflectance to the trained ANN models.

A. DART Simulation

DART is one of the most accurate 3-D RT models for the simulation of remote sensing observations and radiation budget of ground with topography and atmosphere [28], [51], [52]. It simulates the earth-atmosphere radiative coupling and environmental effects in mountainous areas [48]. Its atmospheric RT modeling has been successfully verified with MODerate resolution atmospheric TRANsmission (MODTRAN) [53]. Here, we used DART (version 5.7.9, released on January 28, 2021, downloaded from <https://dart.omp.eu/#/>) with improved accuracy and computational efficiency [48], [54], to simulate HHSA and IISA on sloping terrain. HHSA was simulated by the ratio of the existence (i.e., upward scattered radiation) to irradiance (i.e., total incident radiation) of a horizontal plane above the scene, and IISA equaled to one minus the ratio of the absorbed radiation to the total intercepted radiation provided by the outputs of DART [55].

In DART simulations, the topography was designed as a $30\text{ m} \times 30\text{ m}$ scene (the same size as a "nominal" Landsat pixel) with soil and vegetation, as shown in Fig. 3. Shi and Xiao [26] declared mean errors of albedo when neglecting reflected radiation from neighboring environment was small for low-reflective surface, and Sirguey [56] had similar findings; therefore, the effect of nearby pixels could be neglected in our study. We assumed there was no terrain undulation in the high-resolution satellite pixel, which

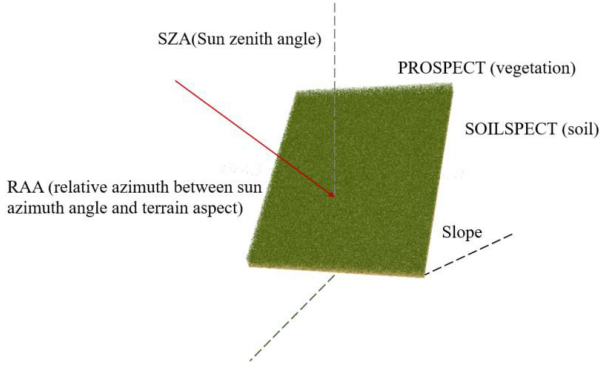


Fig. 3. DART simulation scene.

was called “solo slope” [24]. Thus, we used the so-called “infinite slope” mode that ensures a continuous slope in an infinite landscape [48]. Different topographic conditions were considered by changing the slope and aspect of the scene, while surface and atmospheric properties were also varied to represent different surface and atmospheric conditions. Snow covers, with very noteworthy reflectance from nearby environment [57] and specific simulation conditions [58], were beyond the scope of this study.

Surface BRDF product was not considered as the input for simulation because current available satellite BRDF products were derived from coarse-resolution satellite data, which can contain complex sloping terrain, and the description of BRDF features in mountainous areas remains a challenge [52], [59]. Instead, vegetation and soil’s features on sloping terrain were simulated by the PROSPECT [60] and SOILSPECT [61] models, respectively. Then, we used DART codes for creating the simulation dataset.

Although computing efficiency of DART codes has been continuously improved, carrying out multiple simulations with high-dimension parameters is still time-consuming. Therefore, the space of input parameters was carefully defined to reduce computation time. For example, considering the aerosol conditions in mountain areas [62], we selected three aerosol optical depths AOD values (0.05, 0.2, and 0.4) of the “RURALV23” aerosol model [63]. Gases (water vapor, ozone, etc.) were prescribed by the “USSTD76” model [63]. Following Ma *et al.* [64] and Shi *et al.* [65], we selected “spherical” leaf inclination distribution type. Based on former research [50], [66], [67], we considered four parameters (structure coefficient N , and chlorophyll C_{ab} , dry matter C_m , and leaf water C_w contents) for PROSPECT, and two parameters (ω , b) for SOILSPECT model. Also, a variance-based global sensitivity analysis [23], [68], [69] was performed to determine the intervals of inputting parameters. It decomposed the output variance into fractions of total variance $V(Y)$ to quantify the contribution of each parameter based on the following equation:

$$V(Y) = \sum_{i=1}^n V_i + \sum_{i=1}^n \sum_{j=i+1}^n V_{i,j} \dots + V_{1,2,\dots,n} \quad (3)$$

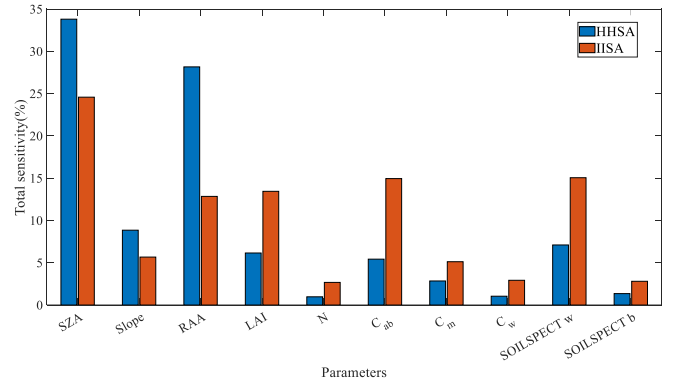


Fig. 4. Total sensitivity analysis for simulation parameters.

TABLE II
INPUT PARAMETERS FOR DART SIMULATION

Parameters	Unit	Range
Sun zenith angle (SZ)	°	0, 10, 20, 30, 40, 50, 60, 70
View zenith angle (VZA)	°	0
Relative angle between sun azimuth angle and terrain’s aspect (RAA)	°	0, 30, 60, 90, 120, 150, 180
Slope	°	5, 10, 20, 30, 40, 50
AOD	-	0.05, 0.2, 0.4
LAI	-	1, 2, 3, 4, 5, 6
Structure coefficient	-	1.5
Chlorophyll $a + b$ content (C_{ab})	$\mu\text{g}/\text{cm}^2$	10, 30, 50, 70
Leaf water content (C_w)	cm	0.01
Dry matter content (C_m)	g/cm^2	0.001, 0.01
SOILSPECT ω	-	0.1, 0.3, 0.5
SOILSPECT b	-	0.5, 2

where n is the number of input variables, V_i is the partial variance of the i th variable, and $V_{i,j}$ is the joint impact of the i th and j th variable variance minus their first-order effects. The total sensitivity index ST_i was defined in the following equation:

$$ST_i = \left(V_i + \sum_{j \neq i} V_{i,j} + \dots + V_{1,2,\dots,n} \right) / V(Y) \quad (4)$$

where a larger ST_i indicates higher importance of the input variable to the output variable.

Fig. 4 shows each variable’s total sensitivity to HHSA and IISA. HHSA depends more on SZ, slope, and RAA than IISA, and less on vegetation and soil properties than IISA. This sensitivity analysis and former studies [23], [50] indicate that IISA and HHSA are sensitive to SZ, slope, RAA, leaf area index (LAI), C_{ab} , and ω . We considered a variation of SOILSPECT b despite its low sensitivity because this low sensitivity is mainly due to dense vegetation (e.g., LAI = 6). Note that scenes with shadow were removed (e.g., SZ = 70°, RAA = 180°, slope = 50°) because shadow areas were out of our study scope. Table II shows the ranges of the selected parameters.

B. Albedo Estimation Method Based on an ANN Model

Machine learning methods have already showed great potential in various domains including remote sensing [70], [71]. Among them, ANNs have a long history and remain popular for modeling nonlinear relationships [72]. In this article, we employed ANNs to establish an empirical relationship between TOA reflectance and surface albedo with the simulation dataset. Using SZA, slope, RAA, and simulated TOA reflectance data as inputs, the ANN model f was defined with a training process that minimized the mean square error between the simulated albedo and predicted albedo. The estimated albedo was

$$\alpha = f(\text{SZA, slope, RAA, TOA reflectance}). \quad (5)$$

To illustrate the need to consider topography as inputs in the model, we also built ANN models without slope and RAA as inputs, and the comparison is shown in Section IV-B.

A fully connected network with four hidden layers (64, 48, 32, and 24 neurons, respectively) was adopted for albedo estimation with a balanced consideration of modeling accuracy and time consumption. The input layer had ten nodes (SZA, slope, RAA, and seven TOA reflectance spectral bands from Landsat 8 OLI). The only output was the estimated surface albedo. A model was constructed for HHSA and also for IISA. All inputs were standardized to zero mean and unit variance to mitigate the scale disagreement of inputs. The ReLU activation function was chosen for powering the ability for solving nonlinear problems in ANN model. Dropout was adopted to prevent overfitting by randomly omitting the feature detectors on each training case [73]. Simulated data were used for training and validation with 75% used for training and 25% to validate models' performance. Shadow areas were excluded [74] because of limited information captured by sensors, and image restoration technology may be a choice [75]. We also used Fmask 4.0 for automated clouds and cloud shadows masking [76].

III. MATERIALS

A. Landsat Data

Landsat satellite series have provided global land observations for over 40 years, with data freely available from the United States Geological Survey (USGS) [77], [78]. The Landsat L1TP dataset offers high geolocation accuracy [79], [80] and accurate radiometric calibration [81], [82]. Data quality was improved with the OLI sensor on-board Landsat 8, launched in 2013. We obtained the Landsat 8 OLI Tier 1 (T1, with highest quality) data from USGS (<https://earthexplorer.usgs.gov/>). The TOA reflectance was derived from the digital numbers using the conversion coefficients included in the Landsat metadata. We used the seven spectral bands of OLI: 0.43–0.45, 0.45–0.51, 0.53–0.59, 0.64–0.67, 0.85–0.88, 1.57–1.65, and 2.11–2.29 μm .

B. SRTM DEM Data

Digital elevation model (DEM) is an effective tool to describe land surface topographic features. Here, Shuttle Radar Topography Mission (SRTM) DEM V003

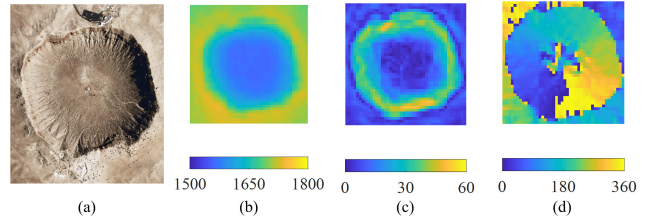


Fig. 5. Meteor Crater. (a) Aerial image (<https://solarsystem.nasa.gov/resources/2257/meteor-crater-arizona-usa>). (b) Elevation (m). (c) Slope angle ($^{\circ}$). (d) Aspect angle ($^{\circ}$).

(<https://search.earthdata.nasa.gov/>) with a 1 arc-second resolution (~ 30 m on the equator) in WGS84 was used to calculate the slope, aspect, incidence angle, and shadows.

Pixel-averaged slope and aspect can be calculated based on DEM data. The illumination conditions (incidence angle i) can be obtained from the following geometric expression [83]:

$$\cos i = \cos \theta_s \cos S + \sin \theta_s \sin S \cos(\varphi_a - \varphi_0) \quad (6)$$

where $\cos i$ is the cosine of the incidence angle, θ_s is the solar zenith angle, S is the slope angle, φ_a is the solar azimuth angle, and φ_0 is the aspect angle of the terrain.

C. In Situ Measurements

In this study, we tried our best to collect *in situ* measurements on sloping terrain with nominal slope greater than 5° from National Tibetan Plateau Data Center, European Fluxes Database Cluster, and Ameriflux for *in situ* measured HHSA, and stations from Chengde for *in situ* measured IISA, as shown in Table III. All cloud-free and snow-free *in situ* measured data were used for validating our method.

D. Experimental Site of Meteorite Crater

Apart from using *in situ* measured data for validation, the exploration of topographic effects on albedo and difference between HHSA and IISA was also made on a sloping landscape. Specific places with relatively homogenous surface properties and comparatively symmetric topographic conditions such as meteor craters were satisfactory choices for in-depth analysis and comparison [91], [92]. In this study, we selected Meteor Crater, AZ, USA (around 35.02°N 111.03°W) as the study area for further evaluation and comparison. The crater basin has a diameter of 1200 m and a depth of 210 m and covered by sparse shrubs and grasses. The image and topographic information of the study area are shown in Fig. 5.

IV. RESULTS

A. Comparison of HHSA and IISA

Differences between HHSA and IISA were analyzed based on the simulated dataset with inputs in Table II. Fig. 6 shows the relationships among slope, SZA, RAA, incidence angle, and albedo for the two albedo definitions. The HHSA varied much more with changes in illumination geometry and terrain slope than the IISA which was relatively stable. Generally, HHSA had large values with large SZA and small RAA, and IISA had large values with large SZA and RAA. The influence

TABLE III
INFORMATION OF IN-SITU MEASUREMENTS FOR VALIDATION

Site name	Latitude/ Longitude(°)	Elevation(m)	Slope/Aspect(°)	Years	References
US-BMM	45.783N/ 110.778W	2324	5.5/194.0	2016-2019	Stoy [84]
IT-Tor	45.844N/ 7.578E	2160	5.5/205.0	2013-2019	Galvagno, et al. [85]
US-xNW	40.054N/ 105.582W	3513	8.1/296.6	2017-2020	Cove Sturtevant, et al. [86]
CH-Frk	46.578N/ 8.421E	2436	12.3/131.3	2013-2014	Georg, et al. [87]
Dayekou	38.556N/ 100.286E	2703	24.4/40.7	2018-2019	Zhao and Zhang [88]
Chengde-1	42.3974N/ 117.3992E	1847	16.3/75.0	2018-2020	
Chengde-2	42.3968N/ 117.3979E	1839	23.7/299.7	2018-2020	
Chengde-3	42.3927N/117.3973E	1865	24.5/206.4	2018-2020	Yan, et al. [22],
Chengde-4	42.3933N/117.3950E	1832	20.6/255.8	2018-2020	Yan, et al. [89],
Chengde-6	42.3957N/ 117.3898E	1770	26.6/180.0	2018-2020	Chu, et al. [90]
Chengde-7	42.3865N/ 117.4005E	1840	37.7/156.9	2018-2020	

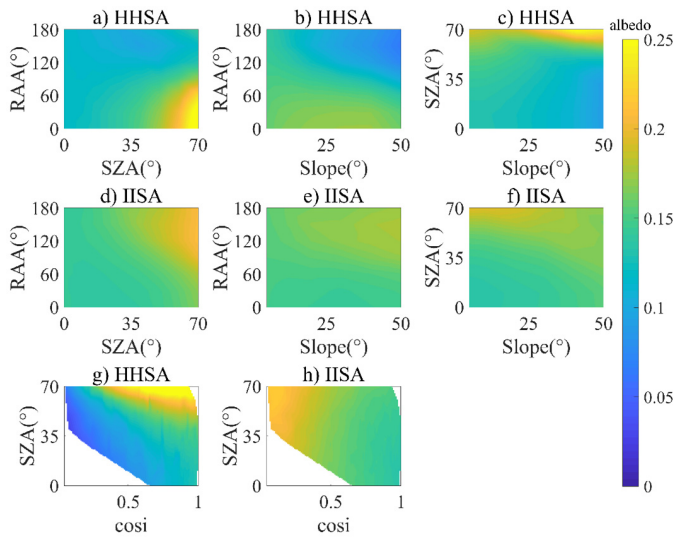


Fig. 6. Variation of (a)–(c) and (g) HHSA and (d)–(f) and (h) IISA with SZA, RAA, slope, and $\cos i$.

of slope was smaller than RAA and SZA for both HHSA and IISA. Meanwhile, the smallest incident angle could be restricted by the SZA. For example, if $SZA = 20^\circ$, the smallest cosine of incidence angle was ≈ 0.34 with slope = 50° , and $RAA = 180^\circ$ [see Fig. 6(g) and (h)]. The comparison in terms of SZA and incidence angle showed the major difference of the two albedos: HHSA was sensitive to both SZA and incidence angle and had large values with high SZA and incidence angle. IISA was seldom influenced by SZA variation, and reached large values with small incidence angle, which was opposite to the behavior of HHSA.

B. ANN Model Training and Validation for Albedo Estimation

Our albedo estimation method was validated with the simulated data. Fig. 7(a) and (b) shows the model training results, and Fig. 7(c) and (d) shows the model validation results using 25% simulation data. ANN models without topography inputs (only input of SZA and TOA reflectance) were also constructed and compared with the validation dataset in Fig. 7(e) and (f). The simulated HHSA values range from

nearly 0 to 0.5, and the IISA values range from about 0.1–0.3 (see Fig. 7). They are mostly clustered around 0.15, which is consistent with the simulated dataset with soil and vegetation. The training results of HHSA model had an R^2 of 0.985, a root mean squared error (RMSE) of 0.008, and a bias of 0; these values were 0.966, 0.007, and 0.001 for the IISA model. The validation results were close to the training results for both models, which stressed their good performance: high R^2 (0.985 and 0.964), low RMSE (0.008 and 0.007), and low bias (-0.001 and 0.001) for HHSA and IISA, respectively. The validation results of the models without topography inputs [see Fig. 7(e) and (f)] were worse, as expected. For HHSA, R^2 decreased from 0.985 to 0.953, and RMSE increased from 0.008 to 0.012. Similarly, for IISA, R^2 decreased from 0.964 to 0.857 and RMSE increased from 0.007 to 0.013. The validation of IISA showed worse results than HHSA without topography inputs, which indicated that IISA depended more on slope and RAA than HHSA in terms of inputting data.

C. Validation Against *in Situ* Measurements

Fig. 8 shows the validation using *in situ* measurements, and colored circles indicate the measurement stations. The comparison of the estimated and measured HHSA and IISA [see Fig. 8(a) and (b)] illustrates the potential of our albedo estimation: RMSE = 0.029, bias = -0.010 , and $R^2 = 0.536$ for HHSA; RMSE = 0.023, bias = -0.001 , and $R^2 = 0.518$ for IISA, which is quite acceptable given the small value of albedo in our study (less than 0.3).

We compared the albedo without topographic consideration to the measured HHSA and IISA: RMSE = 0.029, bias = -0.011 , and $R^2 = 0.37$ for measured HHSA [see Fig. 8(c)]; RMSE = 0.060, bias = 0.029, and $R^2 = 0.119$ for measured IISA [see Fig. 8(d)]. We also cross compared the estimated and measured HHSA and IISA in order to highlight their differences [see Fig. 8(e) and (f)]. It gave greatly larger RMSE and biases: RMSE = 0.060, bias = -0.033 , and $R^2 = 0.058$ for the comparison “estimated IISA–measured HHSA,” and RMSE = 0.072, bias = -0.034 , and $R^2 = 0.017$ for the comparison “estimated HHSA–measured IISA.” Therefore, we get large albedo differences when we consider different reference planes (horizontal or slope-parallel) on sloping terrain. Meanwhile,

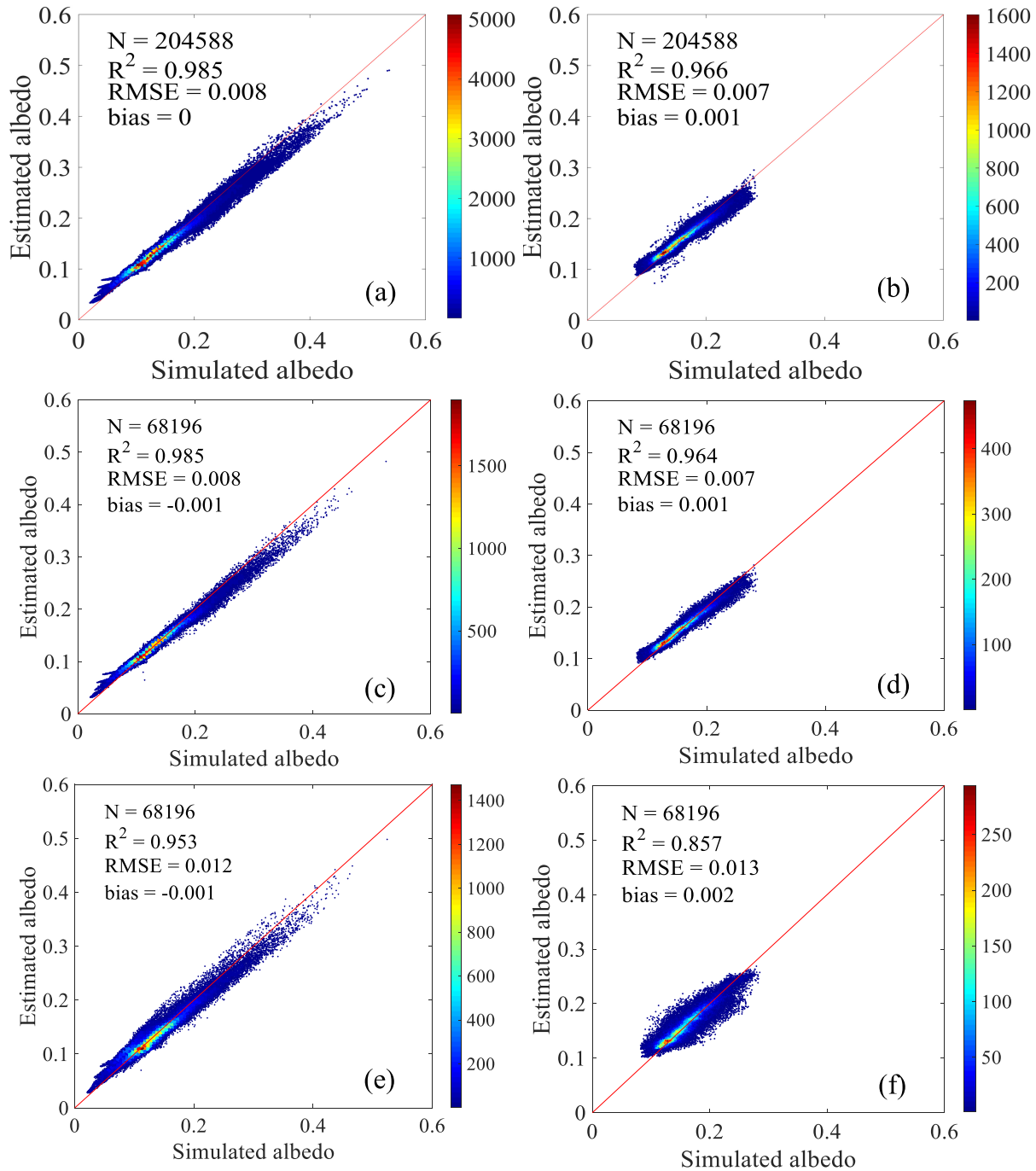


Fig. 7. ANN models’ training and validation results. The color bar shows the point density. Training results of (a) HHSA and (b) IISA. Validation results of (c) HHSA, (d) IISA, (e) HHSA without topography inputs, and (f) IISA without topography inputs.

values of albedo without topographic consideration and HHSA are similar in mountainous area.

D. Analysis of Albedo Estimation in Meteor Crater

Estimated HHSA, IISA, and albedo neglecting topographic effects were compared for the Meteor Crater, AZ, USA. Fig. 9 shows the time series of TOA near-infrared band reflectance and albedo. Terrain with slope less than 5° is shown for display purpose, but focused on the sloping terrain. Fig. 10 shows the relationship between the albedos and incidence angle.

Figs. 9 and 10 further inform on the features of the three albedos. Similar to findings in Section IV-C, the HHSA and albedo neglecting topographic effects had similar values in terms of different topography and times, and they were also similar to the TOA reflectance distributions in Fig. 9. HHSA and albedo neglecting topographic effects were both sensitive to topography, especially for large SZA; for example, their positive correlation with incidence angle was more obvious with larger SZA [see Fig. 10(j)].

The IISA values were stable in the selected images, and topographic effects were difficult to perceive based on visual

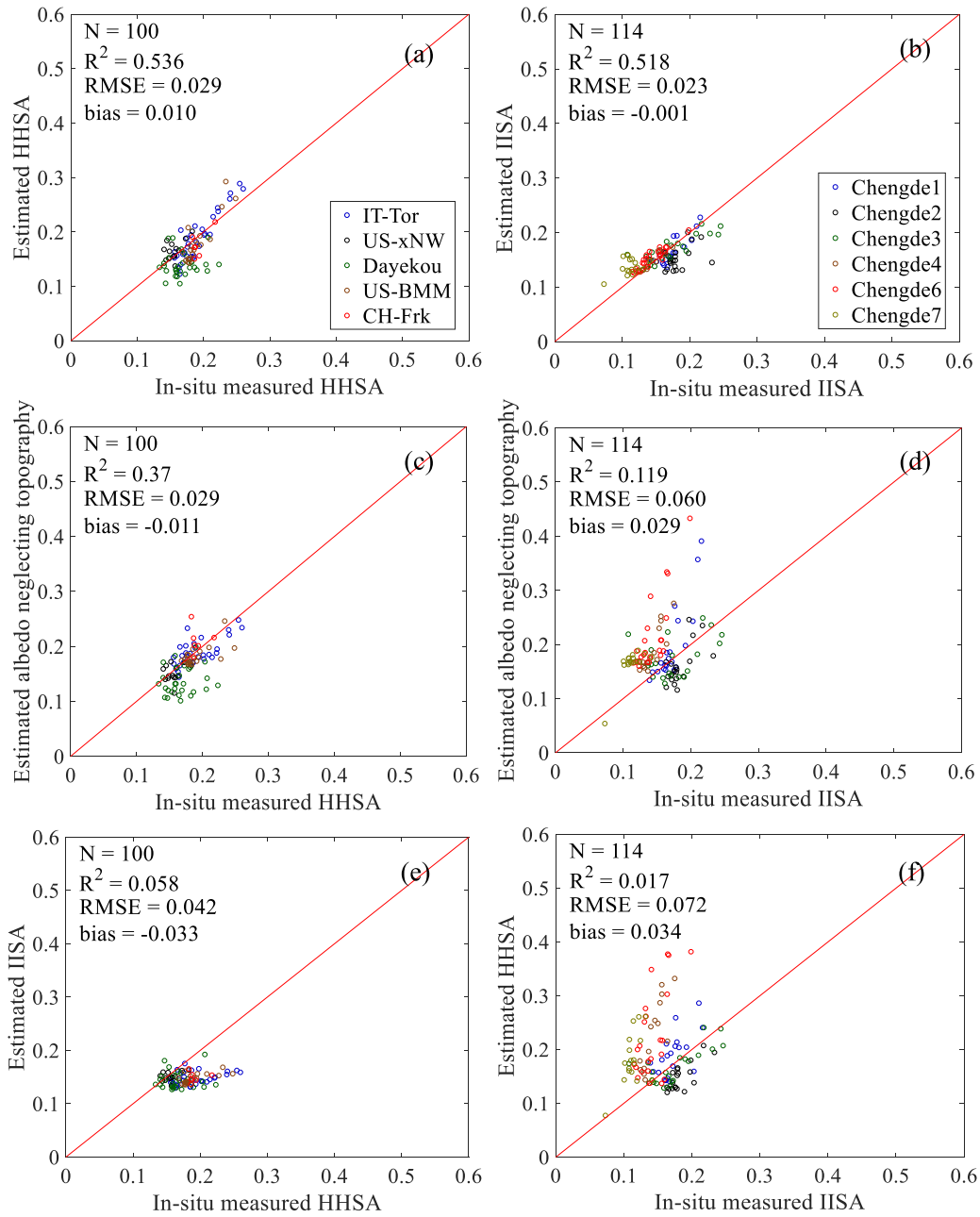


Fig. 8. Validation of estimated surface albedo with *in situ* measurements. (a) Estimated HHSA compared with *in situ* measured HHSA. (b) Estimated IISA compared with *in situ* measured IISA. (c) Estimated albedo without topographic consideration compared with *in situ* measured HHSA. (d) Estimated albedo without topographic consideration compared with *in situ* measured IISA. (e) Estimated IISA compared with *in situ* measured HHSA. (f) Estimated HHSA compared with *in situ* measured IISA. (c) and (e) Same legend as (a), while (d) and (f) have the same legend as (b).

inspection of Fig. 9. In Fig. 10, the correlation of incidence angle and IISA was slightly negative, especially in Fig. 10(j). It was consistent with simulation results in Section IV-A: IISA had opposite trends against HHSA in terms of incidence angle.

E. IISA Mapping Results Example

To evaluate and compare albedo with and without topographic consideration over large areas, we estimated IISA in mountainous areas around Chengde, China (around 41.5°N 118.3°E) in Landsat 8 (Path/Row: 122/031) with small cloud covers. Fig. 11 shows the TOA reflectance false color

composite picture, albedo without topographic consideration, and IISA results for June, September, and November 2017. Flat areas with slope less than 5° are removed in albedo maps. Shadow and cloud cover areas appear as white areas after being masked with algorithms indicated in Section II-B. Fig. 12 shows the comparison of the median values of albedo neglecting topographic effects and estimated IISA in shady (away from the sun) and sunlit (facing the sun) areas in the selected image (path/row: 122/031).

In Fig. 11, topographic effects increase from June to November for both albedos. The characteristics for them

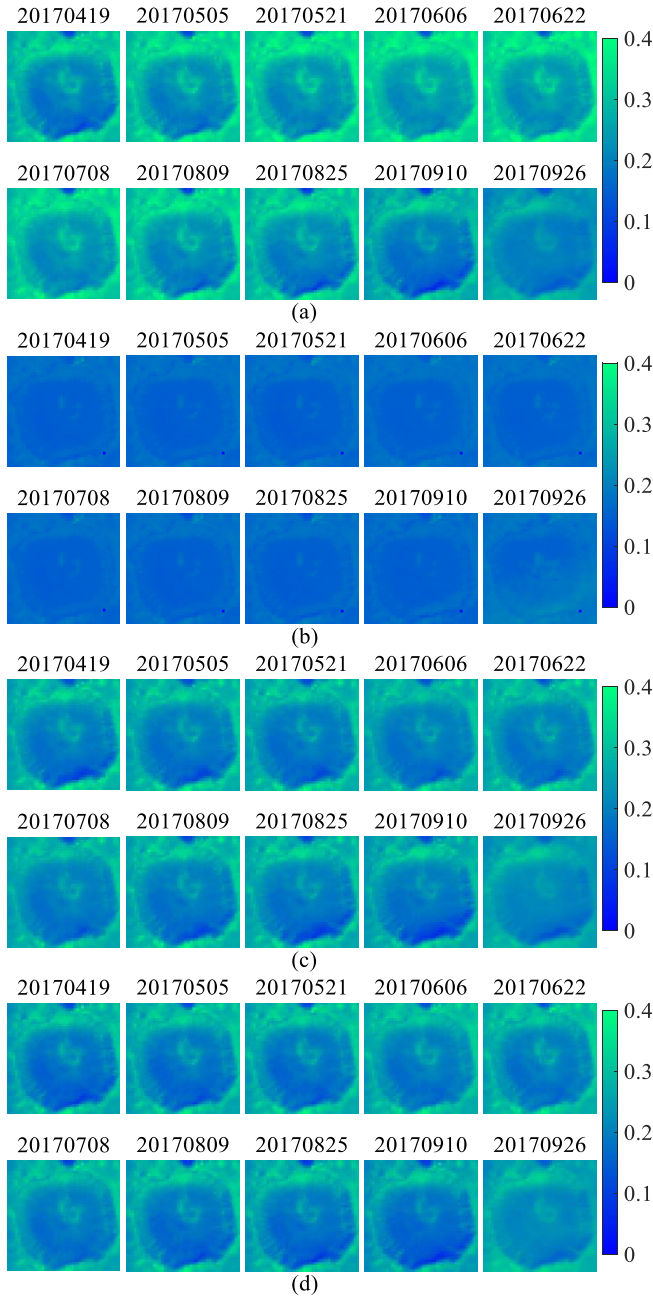


Fig. 9. Time series of TOA reflectance and albedos in Meteor Crater. (a) TOA near-infrared band reflectance (band5). (b) IISA. (c) HHSA. (d) Albedo without topographic consideration.

corresponded with Section IV-D: the value distributions of albedo without topographic consideration were similar as the TOA reflectance, while the high values always appeared in the terrain away from the sun for IISA. IISA was prone to describe the ground changes from June to November: when vegetation withered, and the bare land had relatively high surface albedo. In Fig. 12, IISA was more stable, and the IISA of shady area exceeded that of sunlit area in winter. The difference of sunlit- and shaded-area’s albedo increased from summer to winter when neglecting topographic consideration, which can reach 0.06 (the relative difference is about 50%) in terms of median albedo values.

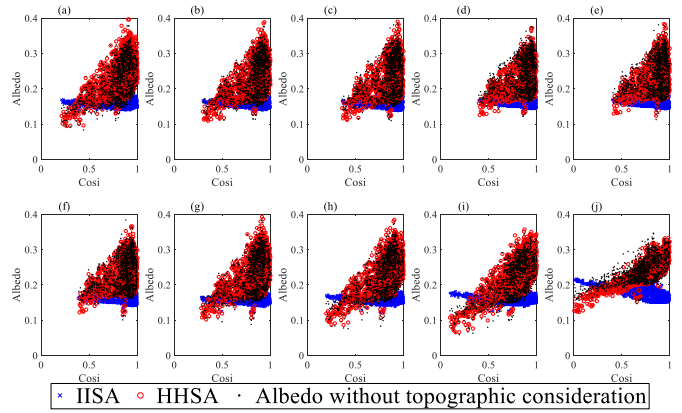


Fig. 10. Relationship of incidence angle and albedos in Meteor Crater. The blue cross is IISA, the red circle is HHSA, and the black point is the albedo without topographic consideration. (a) 20170419. (b) 20170505. (c) 20170521. (d) 20170606. (e) 20170622. (f) 20170708. (g) 20170809. (h) 20170825. (i) 20170910. (j) 20170926.

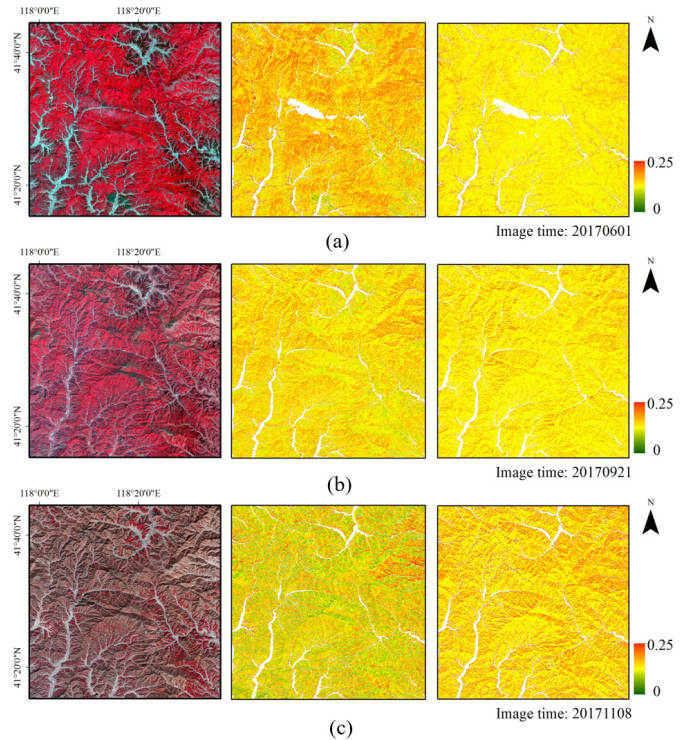


Fig. 11. TOA reflectance and surface albedo in mountain areas for three satellite images. (a) 01/06/2017. (b) 21/09/2017. (c) 8/11/2017. From left to right are TOA reflectance with false color composites, albedo estimates without topographic consideration, and IISA values, respectively. Clouds, shadows, and slope areas less than 5° are masked as white.

V. DISCUSSION

Lin *et al.* [38] reported that the albedo estimation from sloping surface reflectance using mountain RT model was better than the surface reflectance with atmospheric and topographic correction; and over-simplified topographic correction for albedo estimation over rugged terrain would lead to large errors [39]. Meanwhile, the mechanism of the surface albedo has been altered through topographic normalization: it was neither HHSA nor IISA. Therefore, the estimation of surface albedo should couple RT modeling in mountainous areas (e.g., the DART model used in this article). The direct estimation

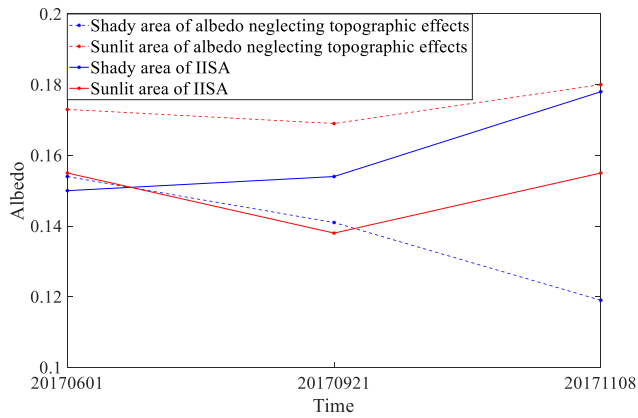


Fig. 12. Median values of albedo neglecting topographic effects and IISA varied with time.

method we developed was simple and straightforward for albedo retrieval with satellite observations, which does not need explicit atmospheric and topographic corrections that are often difficult to be accurately implemented over mountainous regions.

In our study, we combined the atmospheric and surface transfer process using the state-of-the-art 3-D transfer models (DART), and directly retrieved the fine-resolution surface albedo using TOA reflectance. The basic assumption was that there was no subtopography in the fine-resolution pixels. Our method targeted at near-nadir satellites, for satellite with large field of view, the geometric relationship between sun-surface-sensor should be further considered [21]. Our method was both physically sound (based on RT) and simple (input data are easy to obtain and the model is highly efficient). The reasonable results in Figs. 8 and 11 indicated the method's reliability. This study provided a reference for surface albedo estimation in mountains and adopted in-depth analysis in HHSA and IISA, which could advance our knowledge of energy budget and climate change [93], [94]. This study also offered a framework for other surface parameters retrieval (e.g., LAI, net radiation, etc.) in mountainous areas based on 3-D RT models. Further development of consistent retrieval method for multiparameter in mountains could be interesting [36], [95].

There were large differences between HHSA and IISA (see Figs. 6 and 8–10). HHSA was greatly affected by topographic effects, and differences between albedo neglecting topographic effects [46] and HHSA over sloping terrain were much smaller than those between HHSA and IISA. Meanwhile, IISA was less affected by topography, and tended to be more correlated with surface properties (see Fig. 4). It changed with incidence angle in agreement with the variation in albedo of flat areas with SZA [96]. Note that SZA is the incidence angle for horizontal areas, and SZA for flat areas and incidence angle for sloping terrain differ in the reference plane. Because the IISA and HHSA albedos differ in terms of geometry (see Fig. 1), thus, different incident and reflected radiation [28] and downward radiation for horizontal/horizontal measurements could not totally reach the terrain, while the reflected radiation included the radiation from the surrounding pixels. The IISA could capture the incident and reflected radiation of the terrain, and was more inclined to reflect the true properties of the

surface. Therefore, IISA on sloping terrain could reveal the “true albedo” features, and was recommended for applications to characterize the surface inherent properties in terms of continuous land cover. When it comes to single trees and tree clusters, Ramtvedt *et al.* [32] declared that HHSA could be more correlated with the vegetation properties. Owing to various conditions in mountains, the interactions of topography and trees or forest remain a challenge.

IISA over mountain areas was recommended for studying surface energy budget, and some conversion algorithm from *in situ* HHSA measurements to IISA measurements has been proposed [33], [40], [87]. The simple conversion algorithm worked well on *in situ* measurements [33], [40], but its application using remote sensing data seemed difficult: diffuse radiation/direct radiation percentage was the important input, but high accuracy direct/diffuse radiation data in mountainous areas are rare [97]. Therefore, there is a need to develop conversion algorithms from HHSA to IISA to utilize current albedo products for studies in mountains areas.

There were possible factors influencing the validation results of our model (see Fig. 8).

1) Representativeness of simulation dataset. Although we tried to select the typical simulation parameters, it was still difficult to describe diverse ground in the real world and possible uncertainty may be introduced.

2) DEM uncertainty. It was reported that the DEM errors could largely influence shortwave radiation calculations [98], [99], and the accuracy of DEM may impact the validation results in our work.

3) Although the ground data used have been checked with high quality, the sensor tilt of *in situ* measured data may introduce errors into validation [100].

Some limitations and future studies should be noted.

1) Snow cover areas were not studied partly due to the difficulty to simulate snow simulations and significant reflected radiation from surrounding pixels in snow cover area [26], [58].

2) The topographic effect for forest in mountains is largely unclear owing to different tree heights, distributions and mutual shadowing, and insufficient *in situ* measurements; thus, more analysis should be adopted [32], [101]. The energy budget with coupling of topography and forest should be studied to advance our understanding of mountain ecosystem.

3) There were limited ground measurements, especially, “slope-parallel” stations on sloping terrain, which limited validation in our work.

VI. CONCLUSION

There has been an increasing need for surface albedo in mountainous areas. This article mainly solved four problems for albedo estimation in mountains.

1) We designed a proper simulation scene using DART and select appropriate parameters for simulations.

2) We used the ANN model to relate the satellite observations and simulation dataset, which bypassed over complex RT modeling and parameters solving.

3) We proved that it was feasible to estimate both HHSA and IISA using Landsat observations.

4) We systematically compared and analyzed the difference between HHSA, IISA, and albedo neglecting topographic effects.

Based on the global sensitivity analysis and previous studies, major parameters were selected for the simulating scenes with atmosphere and topography by DART, and for inputting simulated data into ANN models for albedo estimation. The final HHSA and IISA were realized by inputting SZA, slope, RAA, and TOA reflectance into the ANN models. Validation against *in situ* measurements verified our proposed method's feasibility: HHSA had an RMSE of 0.029, whereas it was 0.023 for IISA. Our method has a consideration of physical mechanism and easy to apply which could be expanded for regional and global scale. Its good performance also indicates the superiority of 3-D RT models for studies in complicated areas.

Large differences were obtained when comparing HHSA and albedo without topographic consideration against *in situ* IISA measurements (RMSE larger than 0.06). The comparison of HHSA and IISA in the simulation dataset and Meteor Crater deepened our understanding of them on sloping terrain. HHSA was similar to albedo neglecting topographic effects, which was sensitive to the variation of both SZA and incidence angle, and could be greatly affected by topography. In contrast, IISA better reflected the "true" surface properties on sloping terrain; it increased with the incidence angle which is the counterpart of SZA on flat areas. Therefore, IISA is recommended for energy budget studies over sloping terrain, and our resulting IISA images will be of great importance for better understanding of energy budget and climate change in mountainous areas.

ACKNOWLEDGMENT

The authors would like to thank USGS and NASA Earth Science Data Systems for the provision of Landsat data and SRTM DEM. They would also like to thank Prof. Guangjian Yan, Prof. Donghui Xie, and Yingji Zhou for providing valuable *in situ* measurements data in Chengde, and this dataset was provided by the Chengde Remote Sensing Experimental Station, State Key Laboratory of Remote Sensing Sciences. They would also like to thank the anonymous reviewers for their efforts in improving the manuscript. They would also like to thank data support from the National Earth System Science Data Center, National Science and Technology Infrastructure of China (<http://www.geodata.cn>).

REFERENCES

- [1] S. Blyth, *Mountain Watch: Environmental Change & Sustainable Developmental in Mountains*, UNEP/Earthprint, Nairobi, Kenya, 2002.
- [2] FAO, *Mountains are Vital for Our Lives*, I. M. Day, Ed. Food and Agriculture Organization of the United Nations, Rome, Italy, 2018.
- [3] W. W. Immerzeel *et al.*, "Importance and vulnerability of the world's water towers," *Nature*, vol. 577, no. 7790, pp. 364–369, 2020, doi: [10.1038/s41586-019-1822-y](https://doi.org/10.1038/s41586-019-1822-y).
- [4] S. An *et al.*, "Mismatch in elevational shifts between satellite observed vegetation greenness and temperature isolines during 2000–2016 on the Tibetan Plateau," *Global Change Biol.*, vol. 24, no. 11, pp. 5411–5425, 2018, doi: [10.1111/gcb.14432](https://doi.org/10.1111/gcb.14432).
- [5] M. Gao *et al.*, "Divergent changes in the elevational gradient of vegetation activities over the last 30 years," *Nature Commun.*, vol. 10, no. 1, p. 2970, Dec. 2019, doi: [10.1038/s41467-019-11035-w](https://doi.org/10.1038/s41467-019-11035-w).
- [6] N. Pepin *et al.*, "Elevation-dependent warming in mountain regions of the world," *Nature Climate Change*, vol. 5, no. 5, pp. 424–430, May 2015, doi: [10.1038/nclimate2563](https://doi.org/10.1038/nclimate2563).
- [7] W.-L. Lee, K.-N. Liou, C.-C. Wang, Y. Gu, H.-H. Hsu, and J.-L. F. Li, "Impact of 3-D radiation-topography interactions on surface temperature and energy budget over the Tibetan Plateau in winter," *J. Geophys. Res., Atmos.*, vol. 124, no. 3, pp. 1537–1549, 2019, doi: [10.1029/2018JD029592](https://doi.org/10.1029/2018JD029592).
- [8] S. Liang, D. Wang, T. He, and Y. Yu, "Remote sensing of Earth's energy budget: Synthesis and review," *Int. J. Digit. Earth*, vol. 12, no. 7, pp. 737–780, Mar. 2019, doi: [10.1080/17538947.2019.1597189](https://doi.org/10.1080/17538947.2019.1597189).
- [9] S. Liang, A. H. Strahler, and C. Walthall, "Retrieval of land surface albedo from satellite observations: A simulation study," *J. Appl. Meteorol.*, vol. 38, no. 6, pp. 712–725, 1999, doi: [10.1175/1520-0450\(1999\)038<0712:ROLSAF>2.0.CO;2](https://doi.org/10.1175/1520-0450(1999)038<0712:ROLSAF>2.0.CO;2).
- [10] Y. Shuai, J. G. Masek, F. Gao, C. B. Schaaf, and T. He, "An approach for the long-term 30-m land surface snow-free albedo retrieval from historic landsat surface reflectance and MODIS-based *a priori* anisotropy knowledge," *Remote Sens. Environ.*, vol. 152, pp. 467–479, Jul. 2014, doi: [10.1016/j.rse.2014.07.009](https://doi.org/10.1016/j.rse.2014.07.009).
- [11] T. He, S. Liang, D. Wang, H. Wu, Y. Yu, and J. Wang, "Estimation of surface albedo and directional reflectance from moderate resolution imaging spectroradiometer (MODIS) observations," *Remote Sens. Environ.*, vol. 119, pp. 286–300, Apr. 2012, doi: [10.1016/j.rse.2012.01.004](https://doi.org/10.1016/j.rse.2012.01.004).
- [12] C. B. Schaaf *et al.*, "First operational BRDF, albedo nadir reflectance products from MODIS," *Remote Sens. Environ.*, vol. 83, nos. 1–2, pp. 135–148, 2002, doi: [10.1016/S0034-4257\(02\)00091-3](https://doi.org/10.1016/S0034-4257(02)00091-3).
- [13] Y. Qu, Q. Liu, S. Liang, L. Wang, N. Liu, and S. Liu, "Direct-estimation algorithm for mapping daily land-surface broadband albedo from MODIS data," *IEEE Trans. Geosci. Remote Sens.*, vol. 52, no. 2, pp. 907–919, Feb. 2014, doi: [10.1109/TGRS.2013.2245670](https://doi.org/10.1109/TGRS.2013.2245670).
- [14] T. He, S. Liang, and D.-X. Song, "Analysis of global land surface albedo climatology and spatial-temporal variation during 1981–2010 from multiple satellite products," *J. Geophys. Res., Atmos.*, vol. 119, no. 17, pp. 10281–10298, 2014, doi: [10.1002/2014JD021667](https://doi.org/10.1002/2014JD021667).
- [15] Y. Liu *et al.*, "Evaluation of the VIIRS BRDF, Albedo and NBAR products suite and an assessment of continuity with the long term MODIS record," *Remote Sens. Environ.*, vol. 201, pp. 256–274, Nov. 2017, doi: [10.1016/j.rse.2017.09.020](https://doi.org/10.1016/j.rse.2017.09.020).
- [16] B. Mota, N. Gobron, F. Cappucci, and O. Morgan, "Burned area and surface albedo products: Assessment of change consistency at global scale," *Remote Sens. Environ.*, vol. 225, pp. 249–266, May 2019, doi: [10.1016/j.rse.2019.03.001](https://doi.org/10.1016/j.rse.2019.03.001).
- [17] R. Möller, P. Dagsson-Waldhauserova, M. Möller, P. A. Kukla, C. Schneider, and M. T. Gudmundsson, "Persistent albedo reduction on southern Icelandic glaciers due to ashfall from the 2010 Eyjafjallajökull eruption," *Remote Sens. Environ.*, vol. 233, Nov. 2019, Art. no. 111396, doi: [10.1016/j.rse.2019.111396](https://doi.org/10.1016/j.rse.2019.111396).
- [18] J. Houspanossian, R. Giménez, E. Jobbágy, and M. Noretto, "Surface albedo raise in the south American chaco: Combined effects of deforestation and agricultural changes," *Agricult. Forest Meteorol.*, vol. 232, pp. 118–127, Jan. 2017, doi: [10.1016/j.agrformet.2016.08.015](https://doi.org/10.1016/j.agrformet.2016.08.015).
- [19] J. Malle, N. Rutter, C. Webster, G. Mazzotti, L. Wake, and T. Jonas, "Effect of forest canopy structure on wintertime land surface albedo: Evaluating CLM5 simulations with *in-situ* measurements," *J. Geophys. Res., Atmos.*, vol. 126, no. 9, 2021, Art. no. e2020JD034118, doi: [10.1029/2020JD034118](https://doi.org/10.1029/2020JD034118).
- [20] Z. Wang *et al.*, "Monitoring land surface albedo and vegetation dynamics using high spatial and temporal resolution synthetic time series from Landsat and the MODIS BRDF/NBAR/albedo product," *Int. J. Appl. Earth Observ. Geoinf.*, vol. 59, pp. 104–117, Jul. 2017, doi: [10.1016/j.jag.2017.03.008](https://doi.org/10.1016/j.jag.2017.03.008).
- [21] T. Wang, G. Yan, X. Mu, Z. Jiao, L. Chen, and Q. Chu, "Toward operational shortwave radiation modeling and retrieval over rugged Terrain," *Remote Sens. Environ.*, vol. 205, pp. 419–433, Feb. 2018, doi: [10.1016/j.rse.2017.11.006](https://doi.org/10.1016/j.rse.2017.11.006).
- [22] G. Yan *et al.*, "Temporal extrapolation of daily downward shortwave radiation over cloud-free rugged terrains. Part I: Analysis of topographic effects," *IEEE Trans. Geosci. Remote Sens.*, vol. 56, no. 11, pp. 6375–6394, Nov. 2018, doi: [10.1109/TGRS.2018.2838143](https://doi.org/10.1109/TGRS.2018.2838143).
- [23] D. Hao *et al.*, "Sensitivity of coarse-scale snow-free land surface shortwave albedo to topography," *J. Geophys. Res., Atmos.*, vol. 124, no. 16, pp. 9028–9045, Aug. 2019, doi: [10.1029/2019JD030660](https://doi.org/10.1029/2019JD030660).
- [24] J. Wen *et al.*, "Characterizing land surface anisotropic reflectance over rugged terrain: A review of concepts and recent developments," *Remote Sens.*, vol. 10, no. 3, p. 370, Feb. 2018, doi: [10.3390/rs10030370](https://doi.org/10.3390/rs10030370).
- [25] J. G. Wen, Q. Liu, Q. Liu, Q. Xiao, and X. Li, "Scale effect and scale correction of land-surface albedo in rugged terrain," *Int. J. Remote Sens.*, vol. 30, no. 20, pp. 5397–5420, 2009, doi: [10.1080/01431160903130903](https://doi.org/10.1080/01431160903130903).

- [26] H. Shi and Z. Xiao, "Exploring topographic effects on surface parameters over rugged terrains at various spatial scales," *IEEE Trans. Geosci. Remote Sens.*, vol. 60, pp. 1–16, 2022, doi: [10.1109/TGRS.2021.3098607](https://doi.org/10.1109/TGRS.2021.3098607).
- [27] N. Matzinger, M. Andretta, E. van Gorsel, R. Vogt, A. Ohmura, and M. W. Rotach, "Surface radiation budget in an Alpine valley," *Quart. J. Roy. Meteorol. Soc.*, vol. 129, no. 588, pp. 877–895, Jan. 2003, doi: [10.1256/qj.02.44](https://doi.org/10.1256/qj.02.44).
- [28] S. Wu *et al.*, "Characterization of remote sensing albedo over sloped surfaces based on DART simulations and *in situ* observations," *J. Geophys. Res., Atmos.*, vol. 123, no. 16, pp. 8599–8622, Aug. 2018, doi: [10.1029/2018JD028283](https://doi.org/10.1029/2018JD028283).
- [29] T. He, S. Liang, D. Wang, Q. Shi, and M. L. Goulden, "Estimation of high-resolution land surface net shortwave radiation from AVIRIS data: Algorithm development and preliminary results," *Remote Sens. Environ.*, vol. 167, pp. 20–30, Sep. 2015, doi: [10.1016/j.rse.2015.03.021](https://doi.org/10.1016/j.rse.2015.03.021).
- [30] Z. Wang *et al.*, "Early spring post-fire snow albedo dynamics in high latitude boreal forests using landsat-8 OLI data," *Remote Sens. Environ.*, vol. 185, pp. 71–83, Nov. 2016, doi: [10.1016/j.rse.2016.02.059](https://doi.org/10.1016/j.rse.2016.02.059).
- [31] Y. Wang *et al.*, "Surface shortwave net radiation estimation from landsat TM/ETM+ data using four machine learning algorithms," *Remote Sens.*, vol. 11, no. 23, p. 2847, Nov. 2019, doi: [10.3390/rs11232847](https://doi.org/10.3390/rs11232847).
- [32] E. N. Ramtvedt, O. M. Bollandsås, E. Næsset, and T. Gobakken, "Relationships between single-tree mountain birch summertime albedo and vegetation properties," *Agric. Forest Meteorol.*, vol. 307, Sep. 2021, Art. no. 108470, doi: [10.1016/j.agrformet.2021.108470](https://doi.org/10.1016/j.agrformet.2021.108470).
- [33] U. Weiser, M. Olefs, W. Schöner, G. Weyss, and B. Hynek, "Correction of broadband snow albedo measurements affected by unknown slope and sensor tilts," *Cryosphere*, vol. 10, no. 2, pp. 775–790, Apr. 2016, doi: [10.5194/tc-10-775-2016](https://doi.org/10.5194/tc-10-775-2016).
- [34] J. Wen, X. Zhao, Q. Liu, Y. Tang, and B. Dou, "An improved land-surface albedo algorithm with DEM in rugged terrain," *IEEE Geosci. Remote Sens. Lett.*, vol. 11, no. 4, pp. 883–887, Apr. 2014, doi: [10.1109/LGRS.2013.2280696](https://doi.org/10.1109/LGRS.2013.2280696).
- [35] H. Li *et al.*, "Calculation of albedo on complex terrain using MODIS data: A case study in taihang mountain of China," *Environ. Earth Sci.*, vol. 74, no. 7, pp. 6315–6324, Oct. 2015, doi: [10.1007/s12665-015-4656-4](https://doi.org/10.1007/s12665-015-4656-4).
- [36] H. Shi, Z. Xiao, Q. Wang, and D. Wu, "Multiparameter estimation from landsat observations with topographic consideration," *IEEE Trans. Geosci. Remote Sens.*, vol. 59, no. 9, pp. 7353–7369, Sep. 2021, doi: [10.1109/tgrs.2021.3057377](https://doi.org/10.1109/tgrs.2021.3057377).
- [37] G. Traversa, D. Fugazza, A. Senese, and M. Frezzotti, "Landsat 8 OLI broadband albedo validation in Antarctica and Greenland," *Remote Sens.*, vol. 13, no. 4, p. 799, Feb. 2021. [Online]. Available: <https://www.mdpi.com/2072-4292/13/4/799>
- [38] X. Lin, S. Wu, D. Hao, J. Wen, Q. Xiao, and Q. Liu, "Sloping surface reflectance: The best option for satellite-based albedo retrieval over mountainous areas," *IEEE Geosci. Remote Sens. Lett.*, vol. 19, pp. 1–5, 2022, doi: [10.1109/LGRS.2021.3069637](https://doi.org/10.1109/LGRS.2021.3069637).
- [39] Y. Ma, T. He, A. Li, and S. Li, "Evaluation and intercomparison of topographic correction methods based on landsat images and simulated data," *Remote Sens.*, vol. 13, no. 20, p. 4120, Oct. 2021. [Online]. Available: <https://www.mdpi.com/2072-4292/13/20/4120>
- [40] G. Picard *et al.*, "Spectral albedo measurements over snow-covered slopes: Theory and slope effect corrections," *Cryosphere*, vol. 14, no. 5, pp. 1497–1517, May 2020, doi: [10.5194/tc-14-1497-2020](https://doi.org/10.5194/tc-14-1497-2020).
- [41] W. Lucht, C. B. Schaaf, and A. H. Strahler, "An algorithm for the retrieval of albedo from space using semiempirical BRDF models," *IEEE Trans. Geosci. Remote Sens.*, vol. 38, no. 2, pp. 977–998, Mar. 2002, doi: [10.1109/36.841980](https://doi.org/10.1109/36.841980).
- [42] D. Wang, S. Liang, T. He, and Y. Yu, "Direct estimation of land surface albedo from VIIRS data: Algorithm improvement and preliminary validation," *J. Geophys. Res., Atmos.*, vol. 118, no. 22, pp. 12577–12586, 2013, doi: [10.1002/2013JD020417](https://doi.org/10.1002/2013JD020417).
- [43] S. Liang, "A direct algorithm for estimating land surface broadband albedos from MODIS imagery," *IEEE Trans. Geosci. Remote Sens.*, vol. 41, no. 1, pp. 136–145, Jan. 2003, doi: [10.1109/TGRS.2002.807751](https://doi.org/10.1109/TGRS.2002.807751).
- [44] T. He, S. Liang, D. Wang, Q. Shi, and X. Tao, "Estimation of high-resolution land surface shortwave albedo from AVIRIS data," *IEEE J. Sel. Topics Appl. Earth Observ. Remote Sens.*, vol. 7, no. 12, pp. 4919–4928, Dec. 2014, doi: [10.1109/JSTARS.2014.2302234](https://doi.org/10.1109/JSTARS.2014.2302234).
- [45] T. He, S. Liang, D. Wang, X. Chen, D.-X. Song, and B. Jiang, "Land surface albedo estimation from Chinese HJ satellite data based on the direct estimation approach," *Remote Sens.*, vol. 7, no. 5, pp. 5495–5510, May 2015. [Online]. Available: <https://www.mdpi.com/2072-4292/7/5/5495>
- [46] T. He *et al.*, "Evaluating land surface albedo estimation from landsat MSS, TM, ETM+, and OLI data based on the unified direct estimation approach," *Remote Sens. Environ.*, vol. 204, pp. 181–196, Jan. 2018, doi: [10.1016/j.rse.2017.10.031](https://doi.org/10.1016/j.rse.2017.10.031).
- [47] J. Qi *et al.*, "LESS: Large-scale remote sensing data and image simulation framework over heterogeneous 3D scenes," *Remote Sens. Environ.*, vol. 221, pp. 695–706, Feb. 2019, doi: [10.1016/j.rse.2018.11.036](https://doi.org/10.1016/j.rse.2018.11.036).
- [48] Y. Wang, N. Lauret, and J.-P. Gastellu-Etchegorry, "DART radiative transfer modelling for sloping landscapes," *Remote Sens. Environ.*, vol. 247, Sep. 2020, Art. no. 111902, doi: [10.1016/j.rse.2020.111902](https://doi.org/10.1016/j.rse.2020.111902).
- [49] H. Jin *et al.*, "A multiscale assimilation approach to improve fine-resolution leaf area index dynamics," *IEEE Trans. Geosci. Remote Sens.*, vol. 57, no. 10, pp. 8153–8168, Oct. 2019, doi: [10.1109/TGRS.2019.2918548](https://doi.org/10.1109/TGRS.2019.2918548).
- [50] G.-J. Yang, C.-J. Zhao, W.-J. Huang, and J.-H. Wang, "Extension of the Hapke bidirectional reflectance model to retrieve soil water content," *Hydrol. Earth Syst. Sci.*, vol. 15, no. 7, pp. 2317–2326, Jul. 2011, doi: [10.5194/hess-15-2317-2011](https://doi.org/10.5194/hess-15-2317-2011).
- [51] W. Yu *et al.*, "A simulation-based analysis of topographic effects on LAI inversion over sloped terrain," *IEEE J. Sel. Topics Appl. Earth Observ. Remote Sens.*, vol. 13, pp. 794–806, 2020, doi: [10.1109/JSTARS.2020.2970999](https://doi.org/10.1109/JSTARS.2020.2970999).
- [52] S. Wu *et al.*, "The definition of remotely sensed reflectance quantities suitable for rugged terrain," *Remote Sens. Environ.*, vol. 225, pp. 403–415, May 2019, doi: [10.1016/j.rse.2019.01.005](https://doi.org/10.1016/j.rse.2019.01.005).
- [53] E. Grau and J.-P. Gastellu-Etchegorry, "Radiative transfer modeling in the Earth-atmosphere system with DART model," *Remote Sens. Environ.*, vol. 139, pp. 149–170, Dec. 2013, doi: [10.1016/j.rse.2013.07.019](https://doi.org/10.1016/j.rse.2013.07.019).
- [54] J. P. Gastellu-Etchegorry *et al.*, "Recent improvements in the dart model for atmosphere, topography, large landscape, chlorophyll fluorescence, satellite image inversion," in *Proc. IEEE Int. Geosci. Remote Sens. Symp. (IGARSS)*, Sep. 2020, pp. 3455–3458, doi: [10.1109/IGARSS39084.2020.9323458](https://doi.org/10.1109/IGARSS39084.2020.9323458).
- [55] J. P. Gastellu-Etchegorry, *DART User's Manual (5.7.9)*, CESBIO, Toulouse, France, 2021.
- [56] P. Sireguy, "Simple correction of multiple reflection effects in rugged terrain," *Int. J. Remote Sens.*, vol. 30, no. 4, pp. 1075–1081, Feb. 2009, doi: [10.1080/01431160802348101](https://doi.org/10.1080/01431160802348101).
- [57] Q. Chu *et al.*, "Quantitative analysis of terrain reflected solar radiation in snow-covered mountains: A case study in southeastern Tibetan Plateau," *J. Geophys. Res., Atmos.*, vol. 126, no. 11, 2021, Art. no. e2020JD034294, doi: [10.1029/2020JD034294](https://doi.org/10.1029/2020JD034294).
- [58] M. Lamare *et al.*, "Simulating optical top-of-atmosphere radiance satellite images over snow-covered rugged terrain," *Cryosphere*, vol. 14, no. 11, pp. 3995–4020, Nov. 2020, doi: [10.5194/tc-14-3995-2020](https://doi.org/10.5194/tc-14-3995-2020).
- [59] D. Hao *et al.*, "Modeling anisotropic reflectance over composite sloping terrain," *IEEE Trans. Geosci. Remote Sens.*, vol. 56, no. 7, pp. 3903–3923, Jul. 2018, doi: [10.1109/TGRS.2018.2816015](https://doi.org/10.1109/TGRS.2018.2816015).
- [60] J.-B. Féret, A. A. Gitelson, S. D. Noble, and S. Jacquemoud, "PROSPECT-D: Towards modeling leaf optical properties through a complete lifecycle," *Remote Sens. Environ.*, vol. 193, pp. 204–215, May 2017, doi: [10.1016/j.rse.2017.03.004](https://doi.org/10.1016/j.rse.2017.03.004).
- [61] S. Jacquemoud, F. Baret, and J. F. Hanocq, "Modeling spectral and bidirectional soil reflectance," *Remote Sens. Environ.*, vol. 41, nos. 2–3, pp. 123–132, Aug./Sep. 1992, doi: [10.1016/0034-4257\(92\)90072-R](https://doi.org/10.1016/0034-4257(92)90072-R).
- [62] E. Emili *et al.*, "High spatial resolution aerosol retrieval with MAIAC: Application to mountain regions," *J. Geophys. Res., Atmos.*, vol. 116, no. D23, Dec. 2011, doi: [10.1029/2011JD016297](https://doi.org/10.1029/2011JD016297).
- [63] A. Berk *et al.*, "MODTRAN4 radiative transfer modeling for atmospheric correction," SPIE, Bellingham, WA, USA, 1999.
- [64] H. Ma *et al.*, "An optimization approach for estimating multiple land surface and atmospheric variables from the geostationary advanced Himawari imager top-of-atmosphere observations," *IEEE Trans. Geosci. Remote Sens.*, vol. 59, no. 4, pp. 2888–2908, Apr. 2021, doi: [10.1109/TGRS.2020.3007118](https://doi.org/10.1109/TGRS.2020.3007118).
- [65] H. Shi, Z. Xiao, S. Liang, and X. Zhang, "Consistent estimation of multiple parameters from MODIS top of atmosphere reflectance data using a coupled soil-canopy-atmosphere radiative transfer model," *Remote Sens. Environ.*, vol. 184, pp. 40–57, Oct. 2016, doi: [10.1016/j.rse.2016.06.008](https://doi.org/10.1016/j.rse.2016.06.008).
- [66] A. Mousivand, M. Menenti, B. Gorte, and W. Verhoef, "Global sensitivity analysis of the spectral radiance of a soil-vegetation system," *Remote Sens. Environ.*, vol. 145, pp. 131–144, Apr. 2014, doi: [10.1016/j.rse.2014.01.023](https://doi.org/10.1016/j.rse.2014.01.023).

- [67] A. Ding, H. Ma, S. Liang, and T. He, "Extension of the Hapke model to the spectral domain to characterize soil physical properties," *Remote Sens. Environ.*, vol. 269, Feb. 2022, Art. no. 112843, doi: [10.1016/j.rse.2021.112843](https://doi.org/10.1016/j.rse.2021.112843).
- [68] A. Saltelli, "Making best use of model evaluations to compute sensitivity indices," *Comput. Phys. Commun.*, vol. 145, no. 2, pp. 280–297, May 2002.
- [69] J. Verrelst *et al.*, "Emulation of leaf, canopy and atmosphere radiative transfer models for fast global sensitivity analysis," *Remote Sens.*, vol. 8, no. 8, p. 673, Aug. 2016.
- [70] J. Chen, T. He, B. Jiang, and S. Liang, "Estimation of all-sky all-wave daily net radiation at high latitudes from MODIS data," *Remote Sens. Environ.*, vol. 245, Aug. 2020, Art. no. 111842, doi: [10.1016/j.rse.2020.111842](https://doi.org/10.1016/j.rse.2020.111842).
- [71] W. Zhao, S.-B. Duan, A. Li, and G. Yin, "A practical method for reducing terrain effect on land surface temperature using random forest regression," *Remote Sens. Environ.*, vol. 221, pp. 635–649, Feb. 2019, doi: [10.1016/j.rse.2018.12.008](https://doi.org/10.1016/j.rse.2018.12.008).
- [72] K. J. Bergen, P. A. Johnson, M. V. de Hoop, and G. C. Beroza, "Machine learning for data-driven discovery in solid Earth geoscience," *Science*, vol. 363, no. 6433, Mar. 2019, Art. no. eaau0323, doi: [10.1126/science.aau0323](https://doi.org/10.1126/science.aau0323).
- [73] G. E. Hinton, N. Srivastava, A. Krizhevsky, I. Sutskever, and R. R. Salakhutdinov, "Improving neural networks by preventing co-adaptation of feature detectors," 2012, *arXiv:1207.0580*.
- [74] L. Xin, T. Koike, and C. Guodong, "Retrieval of snow reflectance from landsat data in rugged terrain," *Ann. Glaciol.*, vol. 34, pp. 31–37, Jan. 2002, doi: [10.3189/172756402781817635](https://doi.org/10.3189/172756402781817635).
- [75] H. Li, L. Xu, H. Shen, and L. Zhang, "A general variational framework considering cast shadows for the topographic correction of remote sensing imagery," *ISPRS J. Photogramm. Remote Sens.*, vol. 117, pp. 161–171, Jul. 2016, doi: [10.1016/j.isprsjprs.2016.03.021](https://doi.org/10.1016/j.isprsjprs.2016.03.021).
- [76] S. Qiu, Z. Zhu, and B. He, "Fmask 4.0: Improved cloud and cloud shadow detection in Landsats 4–8 and sentinel-2 imagery," *Remote Sens. Environ.*, vol. 231, Sep. 2018, Art. no. 111205, doi: [10.1016/j.rse.2019.05.024](https://doi.org/10.1016/j.rse.2019.05.024).
- [77] C. E. Woodcock *et al.*, "Free access to landsat imagery," *Science*, vol. 320, no. 5879, p. 1011, May 2008, doi: [10.1126/science.320.5879.1011a](https://doi.org/10.1126/science.320.5879.1011a).
- [78] M. A. Wulder *et al.*, "Current status of Landsat program, science, and applications," *Remote Sens. Environ.*, vol. 225, pp. 127–147, May 2019, doi: [10.1016/j.rse.2019.02.015](https://doi.org/10.1016/j.rse.2019.02.015).
- [79] C. J. Tucker, D. M. Grant, and J. D. Dykstra, "NASA's global orthorectified Landsat data set," *Photogramm. Eng. Remote Sens.*, vol. 70, no. 3, pp. 313–322, 2004, doi: [10.14358/PERS.70.3.313](https://doi.org/10.14358/PERS.70.3.313).
- [80] J. C. Storey, M. J. Choate, and K. Lee, "Landsat 8 operational land imager on-orbit geometric calibration and performance," *Remote Sens.*, vol. 6, no. 11, pp. 11127–11152, 2014. [Online]. Available: <https://www.mdpi.com/2072-4292/6/11/11127>
- [81] G. Chander, B. L. Markham, and D. L. Helder, "Summary of current radiometric calibration coefficients for landsat MSS, TM, ETM+, and EO-1 ALI sensors," *Remote Sens. Environ.*, vol. 113, no. 5, pp. 893–903, May 2009, doi: [10.1016/j.rse.2009.01.007](https://doi.org/10.1016/j.rse.2009.01.007).
- [82] J. Lu, T. He, S. Liang, and Y. Zhang, "An automatic radiometric cross-calibration method for wide-angle medium-resolution multispectral satellite sensor using landsat data," *IEEE Trans. Geosci. Remote Sens.*, vol. 60, pp. 1–11, 2022, doi: [10.1109/TGRS.2021.3067672](https://doi.org/10.1109/TGRS.2021.3067672).
- [83] P. M. Teillet, B. Guindon, and D. G. Goodenough, "On the slope-aspect correction of multispectral scanner data," *Can. J. Remote Sens.*, vol. 8, no. 2, pp. 84–106, 1982.
- [84] P. Stoy, *AmeriFlux U.S.-BMM Bangtail Mountain Meadow*. Ameriflux, 2021. [Online]. Available: <https://ameriflux.lbl.gov/sites/siteinfo/US-BMM#data-citation>, doi: [10.17190/AMF/1660338](https://doi.org/10.17190/AMF/1660338).
- [85] M. Galvagno *et al.*, "Phenology and carbon dioxide source/sink strength of a subalpine grassland in response to an exceptionally short snow season," *Environ. Res. Lett.*, vol. 8, no. 2, Jun. 2013, Art. no. 025008, doi: [10.1088/1748-9326/8/2/025008](https://doi.org/10.1088/1748-9326/8/2/025008).
- [86] C. Sturtevant, D. Durden, and S. Metzger, *AmeriFlux U.S.-xNW NEON Niwot Ridge Mountain Research Station (NIWO)*. Ameriflux, 2021. [Online]. Available: <https://ameriflux.lbl.gov/sites/siteinfo/US-xNW#data-citation>, doi: doi.org/10.17190/AMF/1671898.
- [87] W. Georg, H. Albin, N. Georg, S. Katharina, T. Enrico, and Z. Peng, "On the energy balance closure and net radiation in complex terrain," *Agricult. Forest Meteorol.*, vols. 226–227, pp. 37–49, Oct. 2016, doi: [10.1016/j.agrformet.2016.05.012](https://doi.org/10.1016/j.agrformet.2016.05.012).
- [88] C. Zhao and R. Zhang, "Cold and arid research network of Lanzhou university (an observation system of meteorological elements gradient of dayekou station)," Nat. Tibetan Plateau Data Center, Tech. Rep., 2019. [Online]. Available: <http://data.tpdc.ac.cn/en/data/3e049027-3b2d-4fef-8ecd-e24209831e7c/>, doi: [10.11888/Geogra.tpdc.270169](https://doi.org/10.11888/Geogra.tpdc.270169).
- [89] G. Yan *et al.*, "An operational method for validating the downward shortwave radiation over rugged terrains," *IEEE Trans. Geosci. Remote Sens.*, vol. 59, no. 1, pp. 714–731, Jan. 2021, doi: [10.1109/TGRS.2020.2994384](https://doi.org/10.1109/TGRS.2020.2994384).
- [90] Q. Chu *et al.*, "Ground-based radiation observational method in mountainous areas," in *Proc. IEEE Int. Geosci. Remote Sens. Symp.*, Jul. 2019, pp. 8566–8569, doi: [10.1109/IGARSS.2019.8900174](https://doi.org/10.1109/IGARSS.2019.8900174).
- [91] S. W. Hoch and C. D. Whiteman, "Topographic effects on the surface radiation balance in and around Arizona's meteor Crater," *J. Appl. Meteorol. Climatol.*, vol. 49, no. 6, pp. 1114–1128, 2010, doi: [10.1175/2010jamc2353.1](https://doi.org/10.1175/2010jamc2353.1).
- [92] B. Mayer, S. W. Hoch, and C. D. Whiteman, "Validating the MYSTIC three-dimensional radiative transfer model with observations from the complex topography of Arizona's meteor Crater," *Atmos. Chem. Phys.*, vol. 10, no. 18, pp. 8685–8696, Sep. 2010, doi: [10.5194/acp-10-8685-2010](https://doi.org/10.5194/acp-10-8685-2010).
- [93] X. Lin *et al.*, "Spatiotemporal variability of land surface albedo over the Tibet plateau from 2001 to 2019," *Remote Sens.*, vol. 12, no. 7, p. 1188, Apr. 2020, doi: [10.3390/rs12071188](https://doi.org/10.3390/rs12071188).
- [94] L. Zheng, Y. Qi, Z. Qin, X. Xu, and J. Dong, "Assessing albedo dynamics and its environmental controls of grasslands over the Tibetan plateau," *Agricult. Forest Meteorol.*, vol. 307, Sep. 2021, Art. no. 108479, doi: [10.1016/j.agrformet.2021.108479](https://doi.org/10.1016/j.agrformet.2021.108479).
- [95] T. Wang, G. Yan, and L. Chen, "Consistent retrieval methods to estimate land surface shortwave and longwave radiative flux components under clear-sky conditions," *Remote Sens. Environ.*, vol. 124, pp. 61–71, Sep. 2012, doi: [10.1016/j.rse.2012.04.026](https://doi.org/10.1016/j.rse.2012.04.026).
- [96] I. Grant, F. Prata, and R. Cechet, "The impact of the diurnal variation of albedo on the remote sensing of the daily mean albedo of grassland," *J. Appl. Meteorol. Climatol.*, vol. 39, pp. 231–244, Feb. 2000, doi: [10.1175/1520-0450\(2000\)039<0231:TIDTDV>2.0.CO;2](https://doi.org/10.1175/1520-0450(2000)039<0231:TIDTDV>2.0.CO;2).
- [97] Y.-C. Yu, J. Shi, T. Wang, H. Letu, and C. Zhao, "All-sky total and direct surface shortwave downward radiation (SWDR) estimation from satellite: Applications to MODIS and Himawari-8," *Int. J. Appl. Earth Observ. Geoinf.*, vol. 102, Oct. 2021, Art. no. 102380, doi: [10.1016/j.jag.2021.102380](https://doi.org/10.1016/j.jag.2021.102380).
- [98] L. Wang and K. Wang, "Impacts of DEM uncertainty on estimated surface solar radiation and extracted river network," *Bull. Amer. Meteorol. Soc.*, vol. 96, pp. 297–304, Feb. 2015, doi: [10.1175/bams-d-13-00285.1](https://doi.org/10.1175/bams-d-13-00285.1).
- [99] D. Hao *et al.*, "Impacts of DEM geolocation bias on downward surface shortwave radiation estimation over clear-sky rugged terrain: A case study in Dayekou Basin, China," *IEEE Geosci. Remote Sens. Lett.*, vol. 16, no. 1, pp. 10–14, Jan. 2019, doi: [10.1109/LGRS.2018.2868563](https://doi.org/10.1109/LGRS.2018.2868563).
- [100] W. S. Bogren, J. F. Burkhart, and A. Kylling, "Tilt error in cryospheric surface radiation measurements at high latitudes: A model study," *Cryosphere*, vol. 10, no. 2, pp. 613–622, Mar. 2016, doi: [10.5194/tc-10-613-2016](https://doi.org/10.5194/tc-10-613-2016).
- [101] T. Manninen *et al.*, "Airborne measurements of surface albedo and leaf area index of snow-covered boreal forest," *J. Geophys. Res., Atmos.*, vol. 127, no. 1, 2022, Art. no. e2021JD035376, doi: [10.1029/2021JD035376](https://doi.org/10.1029/2021JD035376).



Yichuan Ma received the B.S. degree from the University of Electronic Science and Technology of China (UESTC), Chengdu, China, in 2019. He is currently pursuing the Ph.D. degree with Wuhan University, Wuhan, China.

His main research interests include surface parameters estimation, radiative transfer modeling, and energy budget in mountains.



Tao He (Member, IEEE) received the B.E. degree in photogrammetry and remote sensing from Wuhan University, Wuhan, China, in 2006, and the Ph.D. degree in geography from the University of Maryland, College Park, MD, USA, in 2012.

He is currently a Professor with the School of Remote Sensing and Information Engineering, Wuhan University, and with the Department of Geographical Sciences, University of Maryland. His research interests include surface anisotropy and albedo modeling, surface radiation budget, data fusion of satellite products, and long-term regional and global surface radiation budget analysis.



Shunlin Liang (Fellow, IEEE) received the Ph.D. degree from Boston University, Boston, MA, USA, in 1993.

He is currently a Professor with the Department of Geographical Sciences, University of Maryland at College Park, College Park, MD, USA. He has authored or coauthored over 390 SCI indexed peer-reviewed journal articles, 42 book chapters, and nine special issues on different journals. He has authored/edited seven books and four of which were translated in Chinese, such as *Quantitative Remote*

Sensing of Land Surfaces (Wiley, 2004), *Advances in Land Remote Sensing: System, Modeling, Inversion and Application* (Springer, 2008), *Advanced Remote Sensing: Terrestrial Information Extraction and Applications* (Academic Press, 2012, 2019), *Global LAnd Surface Satellite (GLASS) Products: Algorithms, Validation and Analysis* (Springer, 2013), *Land Surface Observation, Modeling and Data Assimilation* (World Scientific, 2013), and *Earth's Energy Budget* (Elsevier, 2017). He has led a team to develop the Global LAns Surface Satellite (GLASS) products that are publicly available at (www.glass.umd.edu) and widely used. His main research interests focus on estimating land surface variables from satellite data, global satellite product generation, earth's energy balance, and environmental changes.

Dr. Liang was the Editor-in-Chief of the nine-volume books titled *Comprehensive Remote Sensing* (Elsevier, 2017). He was an Associate Editor of the IEEE TRANSACTIONS ON GEOSCIENCE AND REMOTE SENSING. He is currently the Editor-in-Chief of *Science of Remote Sensing*.



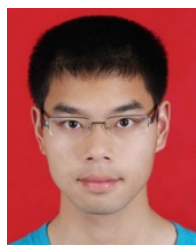
Jianguang Wen received the B.S. degree in geographic information system and the M.S. degree in cartography and geographic information system from the Jilin University of China, Changchun, China, in 2002 and 2005, respectively, and the Ph.D. degree in quantitative remote sensing from the Institute of Remote Sensing Applications, Chinese Academy of Sciences, Beijing, China, in 2008.

He is currently a Researcher with the Aerospace Information Research Institute, Chinese Academy of Sciences. His main research interests include remote sensing radiative transfer mechanism and inversion, and remote sensing experiment in land surface parameters validation.



Jean-Philippe Gastellu-Etchegorry (Member, IEEE) received the B.Sc. degree in electricity from ENSEIHT, Toulouse, France, in 1978, the Aggregation degree in physics from Paris 6 University, Paris, France, in 1981, and the Ph.D. degrees in solar physics and remote sensing from Toulouse III University (UT3), Toulouse, in 1983 and 1989, respectively.

He was with the PUSPICS-Remote Sensing Center, Gadjah Mada University, Yogyakarta, Indonesia, and Southeast Asian Ministers of Education Organization (SEAMEO), Bangkok, Thailand, from 1984 to 1990. He was with the Department of Remote Sensing, Centre d'Etude Spatiale des Rayonnements (CESR), Toulouse, and the Centre d'Etudes Spatiales de la Biosphère (CESBIO), Toulouse, in 1995. He is currently a Professor with UT3. Since 1993, he has been developing the discrete anisotropic radiative transfer (DART) model (<https://dart.omp.eu>). His research interest includes 3-D radiative transfer modeling.



Jiang Chen received the B.S. degree from Huazhong Agricultural University, Wuhan, China, in 2015, and the M.S. degree from Zhejiang University, Hangzhou, China, in 2018. He is currently pursuing the Ph.D. degree in photogrammetry and remote sensing with Wuhan University, Wuhan.

His research interests include quantitative remote sensing and radiative transfer modeling.



Anxin Ding received the B.S. degree from Anhui University of Science and Technology, Huainan, Anhui, China, in 2016, and the M.S. degree from Beijing Normal University, Beijing, China, in 2019. He is currently pursuing the Ph.D. degree with Wuhan University, Wuhan, China.

His research interests include RossThick-LiSparse-Reciprocal (RTLSR) model, snow bidirectional reflectance distribution function (BRDF) model, and snow albedo.



Siqi Feng received the B.S. degree from Wuhan University, Wuhan, China, in 2019, where she is currently pursuing the M.S. degree in photogrammetry and remote sensing.

Her research interest includes the retrieval of surface reflectance and atmospheric parameters from hyperspectral satellite data.